Experimental study on the evolution of mode waves in laminar boundary layer on a large-scale flat plate ⊘

Meikuan Liu (刘美宽) ; Guilai Han (韩桂来) ✉ ; Zonglin Jiang (姜宗林)

Check for updates

View Online   Export Citation   CrossMark

Articles You May Be Interested In

Experimental study on the effects of the cone nose-tip bluntness
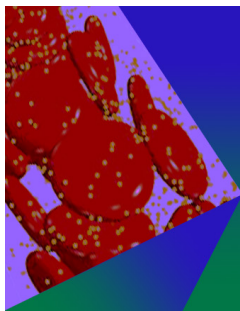
Physics of Fluids (October 2022)

Erratum: "Numerical simulation of the interaction of two shear layers in double backward-facing steps" [Phys. Fluids 31, 056106 (2019)]

Physics of Fluids (August 2019)

Alfvén wave resonances and flow induced by nonlinear Alfvén waves in a stratified atmosphere

AIP Conference Proceedings (July 1996)

Physics of Fluids

Special Topic: Flow and Forensics

Submit Today!   AIP Publishing

Experimental study on the evolution of mode waves in laminar boundary layer on a large-scale flat plate

View Online   Export Citation   CrossMark

Meikuan Liu (刘美宽),[1, 2] (iD) **Guilai Han** (韩桂来),[1, 2,a)] (iD) and **Zonglin Jiang** (姜宗林)[1, 2] (iD)

AFFILIATIONS

[1]State Key Laboratory of High Temperature Gas Dynamics, Institute of Mechanics, Chinese Academy of Sciences, Beijing 100190, China
[2]School of Engineering Science, University of the Chinese Academy of Sciences, Beijing 100049, China

[a)]Author to whom correspondence should be addressed: hanguilai@imech.ac.cn

ABSTRACT

In this research, to study the hypersonic boundary-layer transition, experiments were conducted on a large-scale flat plate with a length of 3.2 m at a zero angle of attack in the hypersonic shock tunnel duplicating flight conditions. Surface-mounted piezoelectric pressure sensors and coaxial thermocouples were, respectively, used to measure the pressure fluctuations and wall heat transfer. The spatial distribution of heat transfer was used to distinguish the transition. Under the test conditions of $Ma = 7.0$, $T_0 = 2120$ K, and $Re_\infty = 6.08 \times 10^5$ m^{-1}, no transition occurred, and under the test conditions of $Ma = 7.0$, $T_0 = 2220$ K, and $Re_\infty = 1.23 \times 10^6$ m^{-1}, the transition position was $s = 2.06$ m. The repeatability of the experiment was found to be good. Furthermore, focus was placed on the spectral and spatial/temporal evolution characteristics of pressure fluctuations in the laminar boundary layer. The experiment captured the three frequency distributions of mode waves in the laminar flow zone. Among the mode waves distributed in the three frequency bands, the low-/high-frequency bands were dominant, and the mid-frequency band exhibited a staged contribution. The amplitude energy percentages of the high- and low-frequency mode waves exhibited opposite trends in both time and space, which means that the disturbance energy will be distributed among the various harmonics in the laminar stage.

Published under an exclusive license by AIP Publishing. https://doi.org/10.1063/5.0075710

I. INTRODUCTION

The boundary-layer transition problem is one of the basic scientific problems that have restricted the breakthrough of hypersonic technology. The hypersonic boundary-layer transition phenomenon is an extremely complex, sensitive, unsteady, non-linear process, and it causes a great change in the boundary-layer flow regime, which in turn significantly affects the local or overall aerodynamics/heating of aircraft. A transitional or turbulent boundary layer may have a heating rate that is three or more times greater than that under laminar conditions.[1] Compared with incompressible flows, hypersonic boundary-layer transition is less understood due to its additional complexities, such as higher instability modes, the applicability of similarity parameters, and the nonlinear coupling of different processes. Most of the difficulty in understanding lies in the large number of factors that affect transition,[2] but that are not independent of each other; factors such as the Mach (Ma) number,[3] freestream disturbance environment, nose bluntness, and wall temperature can all have significant impacts on the location of the transition region.[4] According to many previous studies, there exist different eigenmodes in a hypersonic boundary layer, among which the first- and second-mode instabilities are the basic eigenmodes over a typical geometric model without a pressure gradient.[5] Unlike the conventional first-mode instability, second-mode instability primarily comprises longitudinal acoustic waves reflected between the relative sonic line and the solid wall, and is becoming of crucial importance at high Ma numbers. Additionally, the frequency range of second-mode amplification strongly depends on the local boundary-layer thickness.[6,7] When the eigenmodes increase to a certain amplitude via the receptivity process and linear growth stage, nonlinear interactions between different modes come into effect. As an instability packet convects in the downstream direction, linear and nonlinear growth occur until the pressure fluctuations reach a sufficient magnitude to cause a breakdown, and transition begins.[8]

To fully understand the hypersonic laminar/turbulent boundary-layer transition, researchers have employed theoretical analysis,[9–13]

numerical simulation,[14–24] and experimental methods.[8,25–32] While guidance for the problem of transition may be provided by theoretical studies of laminar instability, the results are not free from criticism due to the use of some simplifying assumptions, the validity of which at high Ma numbers has been questioned. Fedorov[10] reviewed in detail the stability and laminar-turbulent transition in high-speed boundary laminar flow, and emphasized the qualitative characteristics of the disturbance spectrum. In fact, it was not uncomplicated and easy to extend the concept of subsonic stability and transition prediction methods to hypersonic speeds. Lee and Jiang[33] reviewed in detail the basic problems of transition between incompressible and compressible boundary layers. Lee and Chen's[34] review article comprehensively discussed the instability and nonlinear interactions of different instability modes in the hypersonic boundary layer. Liu et al.[35] used the methods of linear stability theory, nonlinear parabolic stability equation, and spatial quadratic instability theory to study the influence of pressure gradient on the secondary instability mechanism essentially by affecting the primary amplitude of the Mack model. Ma and Zhong[36,37] used direct numerical simulation (DNS) and linear stability theory (LST) to study the characteristics of the flat plate boundary-layer wave modes and the receptivity of free-steam fast acoustic waves. They found that in the supersonic boundary layer, in addition to the classical first- and second-order modes, there is also a family of stable wave modes, which play a very important role in the excitation and reception process of the classical modes. Ritos et al.[38] conducted DNS on the hypersonic shock-wave turbulent boundary-layer interactions and showed that the acoustic load is related to the high-pressure gradient area, and the state of the boundary layer affects the pressure fluctuations spectrum. Franko and Lee[39] used DNS to compare the nonlinear development and breakdown to turbulence for different transition mechanisms, stating the oblique mechanism and fundamental breakdown mechanism were relevant. The flat plate DNS results of Leinemann et al.[23] showed that the transition zone of the second mode fundamental breakdown was longer than for the first mode oblique breakdown. Drikakis et al.[40] carried out numerical studies of implicit large eddy simulation (iLES) and DNS for transitional and turbulent boundary layer over a flat plate at hypersonic flow. The results show that the high-order numerical simulation is helpful to adapt and verify the semi-empirical model of the engineering design and acoustic loading of the hypersonic structure. Numerical simulation is one of the important methods by which to study the mechanism of boundary-layer transition; however, it faces two difficulties, namely, the precise and robust capture ability of strong shock waves, and the ability to describe small disturbances with high precision. This situation is further aggravated by the scarcity of experimental data obtained under well-controlled conditions. Due to the numerous factors and complex mechanisms, it is difficult to consider all the factors during theoretical analysis and numerical simulation. Limited by complex conditions, measurement technology and data volume, the accuracy and reliability of the phenomena and data obtained in the flight test[41–43] are greatly compromised. Moreover, it has problems, such as high cost, high risk, and lack of measurement technology. Therefore, wind tunnel experiments will remain one of the most important approaches for research on the mechanism of hypersonic boundary-layer transition in the foreseeable future.

As a typical two-dimensional boundary-layer flow model, the flat plate is very important for boundary-layer transition

investigation. In early studies, researchers used simple configurations, such as sharp cones, blunt cones, flat plates, and blunt plates to study the scientific problems of hypersonic boundary-layer transition. Flood et al.[44] used a flat plate model to capture the instability characteristics of the first and second modes in the boundary layer. Casper et al.[45] carried out a series of hypersonic Mach number boundary-layer transition experiments on a slender cone. The research results showed that with the increase in the Mach number, the dominant position of boundary-layer instability is constantly changing. Sattarzadeh and Fransson[46] used a miniature vortex generator (MVG) to study the characteristics of instability disturbances in the boundary layer of a flat plate, and delayed the occurrence of turbulence by adjusting the base flow in the span direction. Tang et al.[47] studied the development of the second-mode instability within the boundary layer of a flat plate with two-dimensional roughness through a combination of various flow field testing and display methods. Li[48] and Zhang[30] used a flat plate model to systematically explain the influence of glow discharge on the evolution of hypersonic boundary-layer disturbances through wind tunnel experiments. Marineau summarized the results of many hypersonic wind tunnels, focusing on the analysis of various factors affecting the second-mode amplitudes on sharp cones. The above-mentioned wind tunnel test has provided great help to the development of boundary-layer transition and is of great benefit to the understanding of hypersonic boundary-layer transition. Due to the limitation of the experimental equipment, however, early studies usually researched the boundary-layer evolution phenomenon with small models under the conditions of a high unit Reynolds (Re) number and low total temperature T_0. The scale of traditional wind tunnels is small, and the corresponding experimental model is also small. The high unit Reynolds number is usually achieved by reducing the total temperature, which further realizes the boundary-layer transition under the condition of high wall temperature ratio T_w/T_0. The hypersonic shock tunnel duplicating flight conditions (State Key Laboratory of High-Temperature Gas Dynamics of the Chinese Academy of Sciences, hereinafter referred to as the JF-12 hypersonic duplicate tunnel), which has a unique driving method and innovative technology,[49–53] can be used to test the evolution of the boundary layer on large-scale models under the conditions of low unit Re numbers and high total temperature T_0 inflow conditions. The present article primarily focuses on the evolution of the wall fluctuating pressure and heat transfer in a boundary-layer transition experiment.

In this research, experiments were conducted on a large-scale flat plate in the JF-12 hypersonic duplicate tunnel. Surface-mounted piezoelectric pressure sensors and coaxial thermocouples were used to measure the pressure fluctuations and wall heat transfer, respectively. The model employed was a large-scale flat plate (3.2×1.2 m^2), which is the largest flat plate in the world. The truest boundary-layer transition evolution process was restored by reproducing the flow field closest to that during real flight and the model closest to the scale of the aircraft. In this work, the spatial distribution of heat transfer was used to distinguish the transition. The spectral characteristics and spatial/temporal evolution characteristics of pressure fluctuations in the laminar flow region of the boundary layer were then investigated.

II. EXPERIMENTAL FACILITIES AND PROCEDURE

A. Shock tunnel and test conditions

A shock tunnel is one of the main ground simulation equipment for hypersonic aerodynamics due to its large experimental range, strong experimental ability, large model scale, and multiple measurement methods. In this study, experiments were conducted in the JF-12 hypersonic duplicate tunnel,[49–52] a schematic of which is presented in Fig. 1(a). The total length of the wind tunnel is 265 m and includes six main parts: a damping section, driver section, driven section, nozzle, test section, and E-shaped vacuum tank. The driver section is filled with a gaseous reactive mixture, which is typically composed of oxygen and hydrogen. Strong incident shock waves are then easily generated in the driven section by detonation product gases at high temperatures and pressures after simultaneously igniting the reactive mixtures. As depicted in Fig. 1(b), the JF-12 hypersonic duplicate tunnel is a large-scale shock tunnel, and it can be used to simulate integrated vehicle/engine conditions, and provides a reliable ground test method for the key technical research of hypersonic vehicles and the basic research of high-temperature aerodynamics. The JF-12 hypersonic duplicate tunnel can reproduce hypersonic flight conditions at a height of 25–50 km and Ma = 5–9. The total temperature is 1500–3500 K, and the total pressure is 2–12 MPa. Its nozzle diameter is 2.5 m, the effective test time is longer than 100 ms, and the test gas is air; the noise level of the wind tunnel was less than 2%, other details are available in a previous publication.[53]

Considering the model characteristics and the flow-field conditions of the JF-12 hypersonic duplicate tunnel, to effectively capture the transition characteristics of the flat plate boundary layer, the test flow field was selected with the conditions reported in Table I. The three tests included two cases. Tests were conducted at two different nozzle reservoir enthalpies of approximately 2.40 and 2.53 MJ kg^{-1}; these conditions are, respectively, referred to as case I and case II.
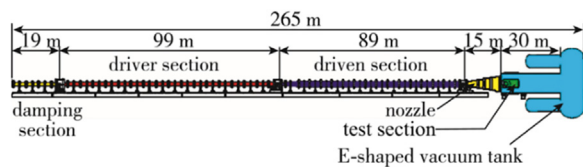
(a)

(b)

FIG. 1. (a) The schematic and (b) an image of the JF-12 hypersonic duplicate tunnel.

TABLE I. Reservoir and freestream conditions for cases I and II. Re = unit Reynolds number, ρ = density, U = velocity, T = temperature, Ma = Mach number, h = enthalpy, P = pressure. The subscripts "0" and "∞" refer to the conditions in the nozzle reservoir and the freestream, respectively. The model wall temperature T_w = 288 K (ambient).

Parameter	Case I	Case II
Re_∞ ($\times 10^6$ m^{-1})	0.61	1.23
ρ_∞ ($\times 10^{-3}$ kg m^{-3})	4.25	8.68
U_∞ (km s^{-1})	2.10	2.14
T_∞ (K)	225	233
Ma$_\infty$	7.0	7.0
h_0 (MJ kg^{-1})	2.44	2.53
T_0 (K)	2120	2220
P_0 (MPa)	1.53	3.28

The typical values of the flow parameters for the reservoir and freestream conditions are presented in Table I.

B. Model details

The experimental model was a large-scale leading-edge flat plate (the diameter of the leading-edge bluntness is less than 0.3 mm). As illustrated in Fig. 2, the model width of 1.2 m was chosen to avoid disturbing the flow field in the central region of the plate model. The model length of 3.2 m ensured that dense sensors could be arranged to achieve a high spatial resolution. Figure 2(a) is a schematic diagram of the installation of the flat plate model in the wind tunnel. The flat plate was installed in the center of the wind tunnel flow field. As depicted in Fig. 2(b), it is a top view of the large-scale flat plate installed in the JF-12 hypersonic duplicate tunnel. To ensure that the detachment condition was not approached,[54] as shown in Fig. 2(c), a wedge angle of 15° was chosen.

Two hundred and forty coaxial thermocouple sensors and eight PCB sensors were arranged along the central region of the flat plate. Figure 2(d) exhibits the layout of sensors on the large-scale flat plate; eight PCB sensors were arranged on one side of the centerline [as indicated by the blue dots in Fig. 2(d)] and were numbered ch1–ch8 from upstream to downstream of the flow field. The distances between these sensors and the theoretical plate sharp leading-edge are presented in Table II. The entire plate model was divided into four parts, each of which had many coaxial thermocouple sensors arranged along the centerline. The front part of the model was equipped with five sensors (red dots) followed by three identical plates; the three downstream plates included a plate with densely arranged sensors every 5 mm, and two plates with relatively sparsely arranged sensors every 50 mm. The three downstream plates could be replaced according to different incoming flow conditions and transition positions to capture the evolution of heat transfer during the transition process. To ensure that the surface roughness of the model met the experimental requirements and to avoid the influence of lateral heat transfer on the sensor measurement,[55] the entire flat plate model was made of stainless steel, and the four plates were polished after assembly to minimize the thickness of the connecting steps between the plates.
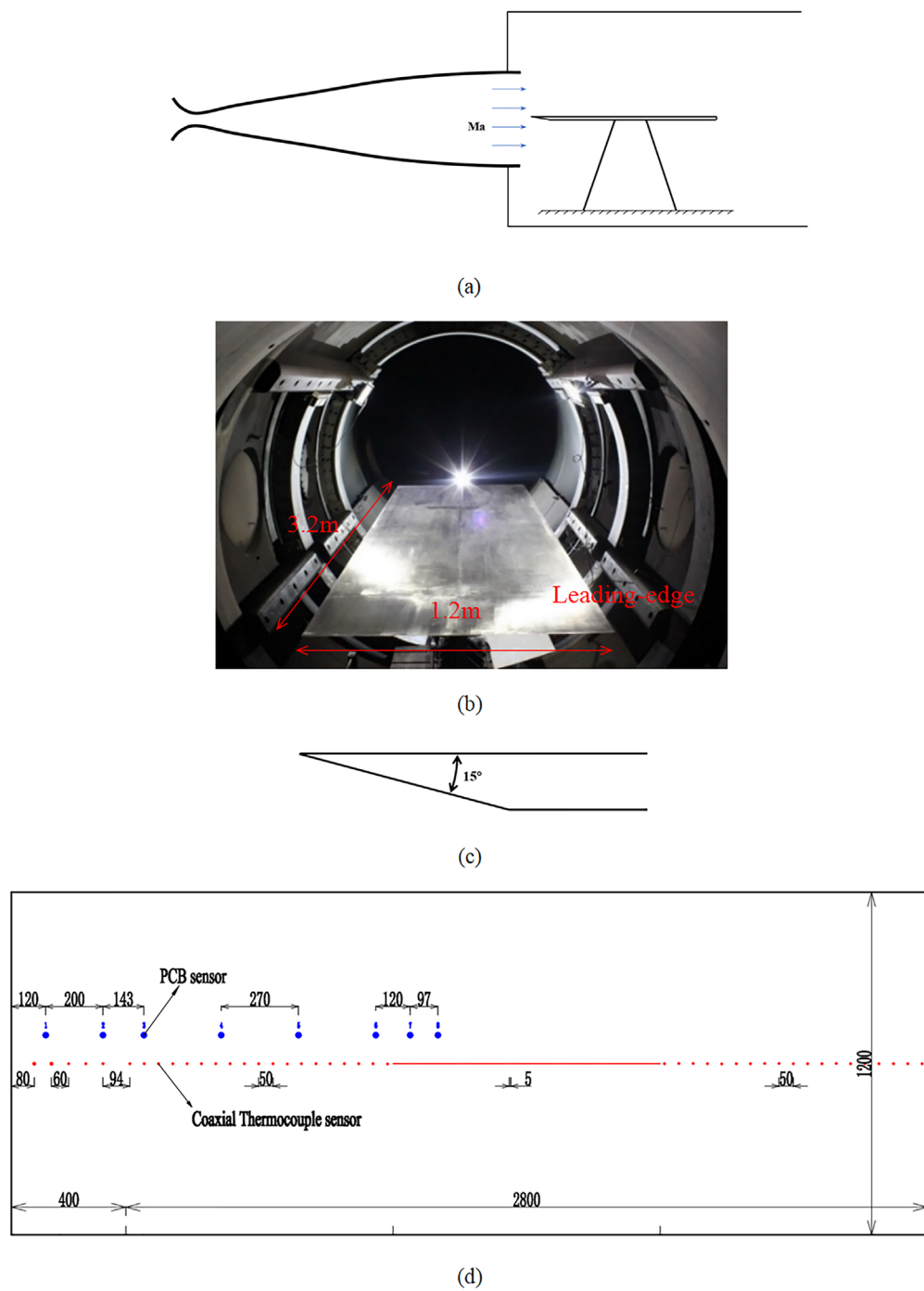
(a)

(b)

(c)

(d)

FIG. 2. Large-scale flat-plate model details: (a) the schematic of the model; (b) a top view of the large-scale flat plate was installed in the JF-12 hypersonic duplicate tunnel; (c) the leading-edge configurations; and (d) the layout of sensors on the model, in which red dots represent coaxial thermocouple sensors and blue dots represent PCB sensors.

C. Instrumentation

Suitable measurement techniques were developed for the shock tunnel based on its own characteristics (high air velocity, low gas density, and millisecond test time) to investigate the hypersonic boundary-layer transition. Moreover, piezoelectric pressure sensors, PCB 132B38, were used to measure the pressure fluctuations along the flat plate. The sensor output was high-pass filtered with a 3-dB cutoff frequency at 11 kHz. The sensor is a high-frequency piezoelectric

TABLE II. Distances between the PCB sensors and the theoretical plate sharp leading-edge.

Sensor	ch1	ch2	ch3	ch4	ch5	ch6	ch8
Location (m)	0.120	0.320	0.463	0.733	1.003	1.273	1.490

time-of-arrival sensor with a resolution of 7 Pa and a resonance frequency of greater than 1 MHz. In addition, the diameter of the sensor is 3.18 mm, as shown in Fig. 3, but the effective sensing area is merely about 0.622 mm². The size of the pressure transducer affects the accuracy of the measurement, that is, the pressure wavelength smaller than the sensor size cannot be effectively measured. Many researchers [Corcos,[56] Willmarth,[57,58] and Lueptow[59]] have proposed reliable methods to provide correction factors for the frequencies measured in the boundary layer. In the current research, the large-scale flat plate model combined with the low unit Reynolds number has reached the high spatial resolution of the instability waves. Many previous studies,[60–62] in different wind tunnel facilities, have used this type of high-frequency response sensor to effectively collect instability waves in the hypersonic boundary layer. Furthermore, the evolution of instability waves was further analyzed through the spatial distribution and response characteristics of different sensors.

The heat transfer was determined using high-precision coaxial nickel–chromium constantan (type "E") surface junction thermocouple sensors. Figure 4(a) depicts the end face of a coaxial thermocouple sensor with a diameter of 1.4 mm. The principle of temperature measurement is based on the Seebeck effect. As shown in Fig. 4(b), at a certain temperature, the free electron densities in two different conductor materials will be different. At their junctions, due to free electron diffusion, a diffusive electromotive force is generated. The principle of using coaxial thermocouples to measure heat transfer is derived from the one-dimensional infinite heat conduction problem via Laplace transformation to obtain the relationship between the end heat transfer and the temperature change. To further improve the performance of the coaxial thermocouple and reduce the response time of the sensor, the active junction of these thermocouples was obtained by grinding their front surfaces to locally bypass the electrical insulation.[55,63,64] The small mass of the active thermal junction ensured a response time on the order microseconds, which is particularly suited for the study of hypersonic flows in short-duration tunnels.
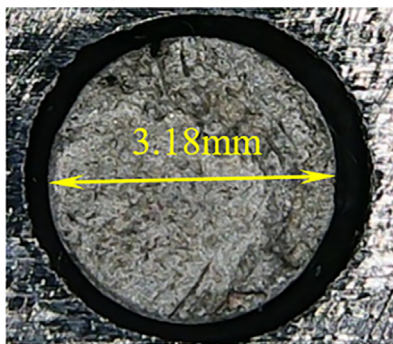
FIG. 3. A PCB sensor mounted on the flat plate model; an O-shaped rubber ring was used to isolate the sensor and model.
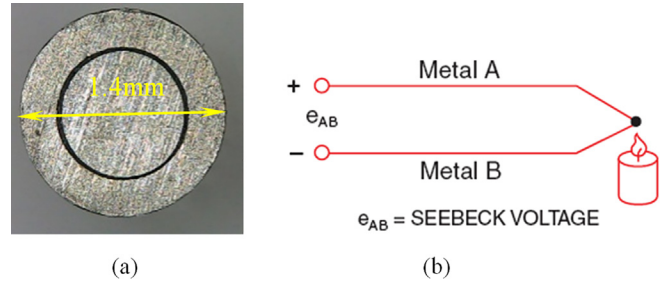
FIG. 4. Details of the coaxial thermocouple sensors: (a) the end face of a 1.4 mm coaxial thermocouple sensor and (b) the schematic of the Seebeck effect.

D. Data acquisition

The data acquisition systems located at each physical quantity to be measured were different, but provided similar high-speed sampling and antialiasing over many channels. The experimental heat transfer data were acquired at 200 kHz using a National Instruments 18–28-bit PXIe-4309 module mounted on a PXI-1085 chassis. The heat transfer was inferred from the temperature variation with time, as measured by the thermocouple sensors. Figure 5 presents a typical temperature trace obtained by the acquisition system on the large-scale flat plate in the JF-12 hypersonic duplicate tunnel. The original temperature signal will be sorted and filtered before integration, and then averaged to obtain a smoother signal.

The wall surface heat transfer q_w can be calculated by measuring the temperature trace $T_w(t)$ via the following equation:[65]

$$q_w(t_j) = 2\frac{\sqrt{\rho c k}}{\sqrt{\pi}}\sum_{i=1}^{j}\frac{T_w(t_i) - T_w(t_{i-1})}{\sqrt{t_j - t_i} + \sqrt{t_j - t_{i-1}}}, \qquad (1)$$

where ρ, c, and k, respectively, denote the density, specific heat capacity, and thermal conductivity of the sensor node material, and T_w and t are the measured node temperature and corresponding time,
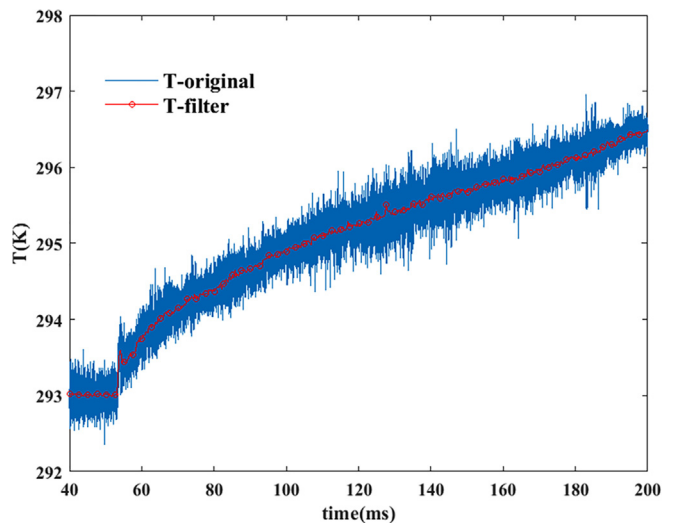
FIG. 5. A typical temperature trace in the JF-12 hypersonic duplicate tunnel (sampling frequency: 200 kHz and filtering: 10 kHz low-pass filter).
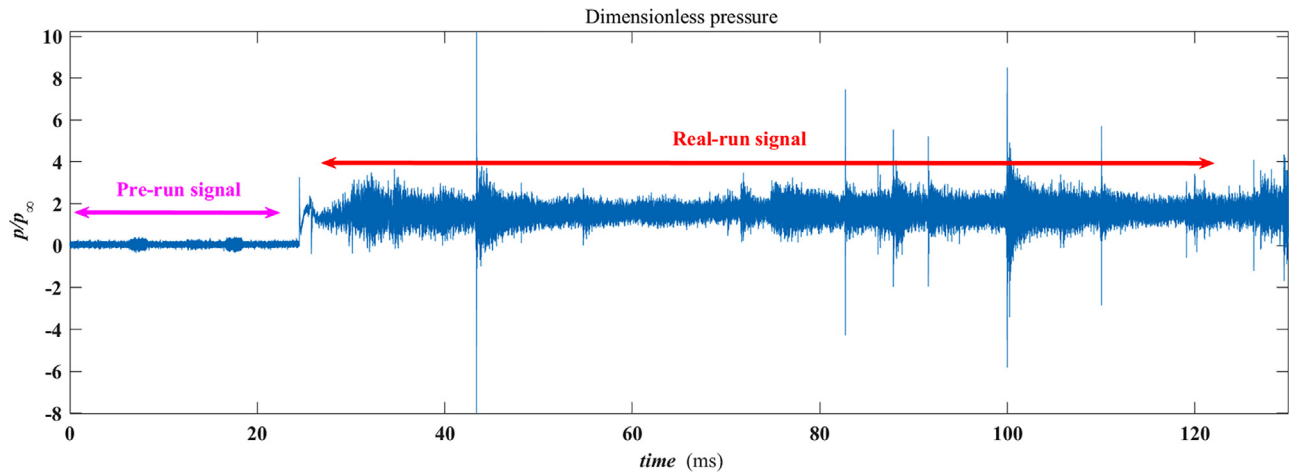
FIG. 6. A typical pressure trace in the JF-12 hypersonic duplicate tunnel (sampling frequency: 3.5 MHz and filtering: 11–1000 kHz bandpass filter).

respectively. The thermal properties of the thermocouples were determined by the manufacturer. The parameters of the coaxial thermocouple sensor were obtained via experimental measurements, $\sqrt{\rho c k} = 7950 \left(\mathrm{W} \sqrt{\mathrm{s}} / \mathrm{m}^2 \, \mathrm{K} \right)$.

The PCB 132B38 sensors all ran through a PCB 482C05 signal conditioner that provided constant-current excitation to the built-in sensor amplifier. Data were acquired using a National Instruments PXIe-1092 chassis with 16-bit PXIe-6124 modules. In this research, the collected original signal was converted into a pressure signal according to the sensitivity of the sensor, and the time traces were then normalized by the edge pressure of the boundary layer. Figure 6 presents a typical pressure trace curve obtained in the JF-12 hypersonic duplicate tunnel, which includes the pre-run signal segment before the wind tunnel was started and the actual acquired signal segment within the effective time of the wind tunnel.

The sampling frequency of the sensors was 3.5 MHz, and 130 ms of data were recorded for each experimental run. The power spectral densities (PSDs) were then calculated for 100 ms samples using Welch's method. The original signal was filtered by a 6th-order Butterworth bandpass filter set at 11–1000 kHz. The signal processing adopted the Hamming window, which has a better frequency resolution and less spectrum leakage. Hamming windows with 50% overlap and a fast Fourier transform (FFT) length of 4096 points were used, which resulted in a frequency resolution of 0.85 kHz. Approximately 170 FFTs were averaged. The obtained results are presented in Fig. 7, and the actual collected spectrum was much larger than the pre-run signal spectrum, indicating that the signal-to-noise ratio (SNR) of the signal itself was very high and the collected signal was effective.

III. RESULTS AND DISCUSSION

A. Heat transfer and transition location

Due to its good repeatability, reliability, and accuracy, the distribution of the wall heat transfer along a model is commonly used to determine the transition location. In this paper, the start of transition is defined as the location at which an increase in heat transfer was first observed. The signals collected by the thermocouple sensors were processed within the effective time, and the wall heat transfer in the

boundary layer of the large-scale flat plate was then obtained. As presented in Fig. 8, the abscissa s represents the distance between these sensors and the theoretical sharp leading-edge flat plate, and the ordinate q_w represents the heat transfer. The uncertainty of the heat transfer data are 6%. In case I, as shown in Fig. 8(a), the heat transfer exhibited no obvious jump, and it can be judged that the entire flat plate was in full laminar flow; in case II, as shown in Fig. 8(b), the wall heat transfer started to takeoff at $s = 2.05$ m (corresponding to $Re_x = 2.6 \times 10^6$), and it can be judged that the transition occurred under this condition.

The incoming Ma numbers of cases I and II were the same, and the total temperature was almost the same; the only difference was the value of Re_∞. Therefore, the results of the three experiments are dimensionless in the following expression:[4]

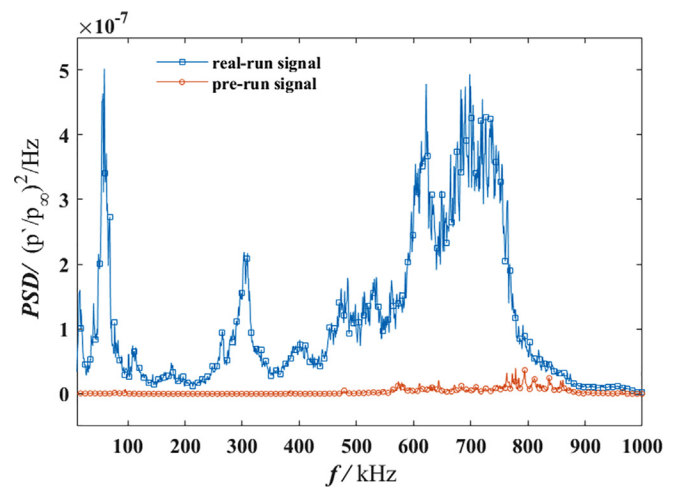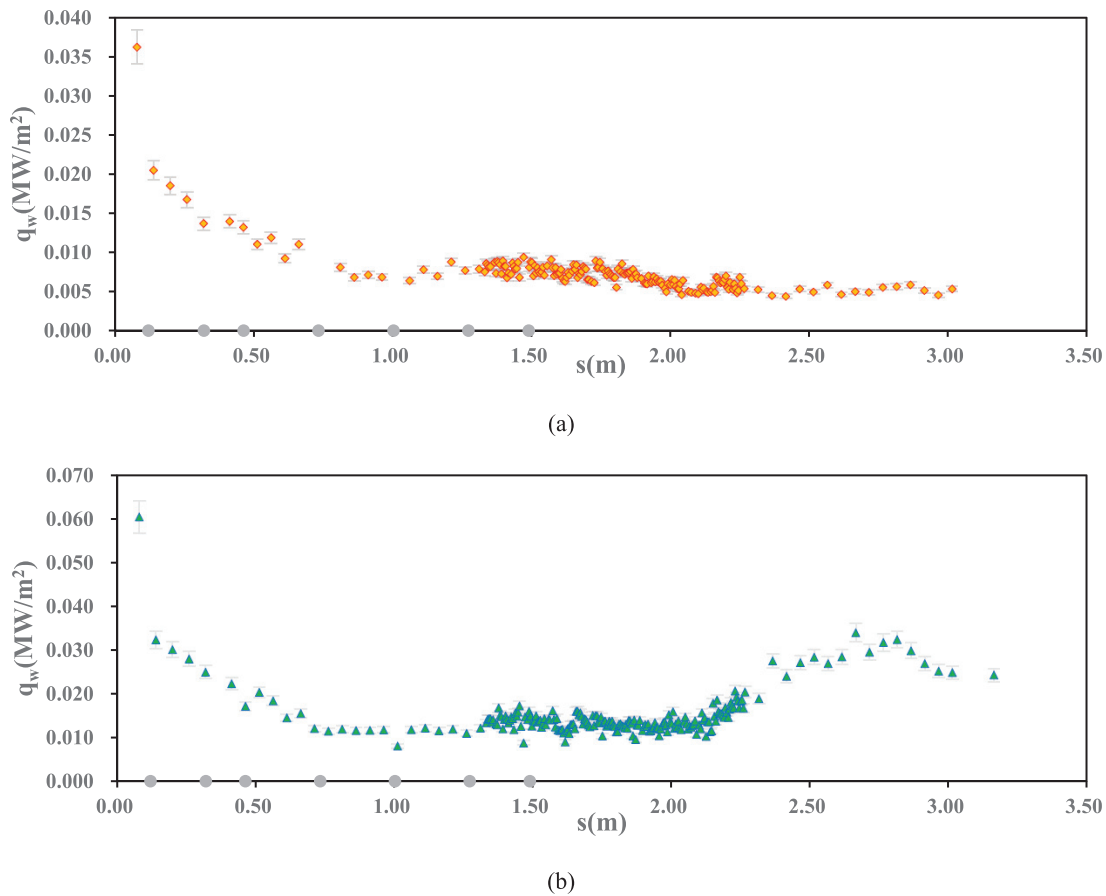$$St = \frac{q_w}{\rho_e U_e (h_r - h_w)}, \tag{2}$$

FIG. 7. Real-run and pre-run signal PSDs with a high SNR.

FIG. 8. The spatial distribution of the heat transfer: (a) case I: Ma $= 7.0$, $T_0 =2120$ K, $Re_\infty = 6.08 \times 10^5$; and (b) case II: Ma $= 7.0$, $T_0 = 2220$ K, $Re_\infty = 1.23 \times 10^6$.

where $h_r = h_0 + \frac{1}{2}\left(\sqrt{Pr} - 1\right)U_e^2$ is the recovery enthalpy, $h_w = c_p T_w$ is the enthalpy at the wall, and c_p is the specific heat at constant pressure. The spatial resolutions of the heat transfer sensors were different; in order to clearly display the results, the corresponding dimensionless heat transfer values are given at a fixed spatial resolution of 50 mm. As revealed by Fig. 9, in which the abscissa Re_x is the local Reynolds number and the ordinate is the dimensionless heat transfer coefficient St, by making the heat transfer dimensionless, it can be concluded that the dimensionless heat transfer coefficients St in the three experiments agreed well in the laminar stage, and the change in Re_∞ did not affect the distribution of the heat transfer coefficient in the laminar stage. According to the experimental data of the two runs of case II, it can be inferred that the JF-12 hypersonic duplicate tunnel ran stably and the test repeatability was good. Furthermore, in the laminar stage, the error between the experimental heat transfer values and the theoretical solution was within 15%, and in the turbulent stage, the error was within 25%.

B. Mode waves in the boundary layer

The transition results of Sec. III A are mainly used to partition the flow field and highlight trends, but lack the discussion of the internal mechanism of boundary-layer transition. Therefore, in order to better understand the mechanism of transition, the PCB pressure sensors were used to characterize the spectral content and temporal/ spatial evolutions of the wall pressure fluctuations below 1000 kHz. The boundary-layer stability characteristics of the flat plate were determined via the data processing methodology outlined in Sec. II D. As exhibited in Fig. 8, the gray point on the abscissa represents the position at which the PCB sensor was installed. By combining the heat transfer results and the positions of the PCB sensors, in all the experimental runs the PCB sensors were distributed in the laminar stage. As presented in Fig. 10, the frequency spectrum can be divided into three frequency bands. In the subsequent analysis, the frequency component of 11–200 kHz was called the low-frequency band, the frequency component of 200–400 kHz was called the mid-frequency band, and the frequency component beyond 400 kHz was called the high-frequency band. In case I, the low-frequency band was concentrated in the range of 13–93 kHz, the middle frequency band was concentrated in the range of 250–320 kHz, the high-frequency band was concentrated in the range of 640–780 kHz, and the dominant frequency bands were low-frequency bands. In case II, the low-frequency band was concentrated in the range of 12–94 kHz, the middle frequency band was concentrated in the range of 250–350 kHz, the high-frequency band was
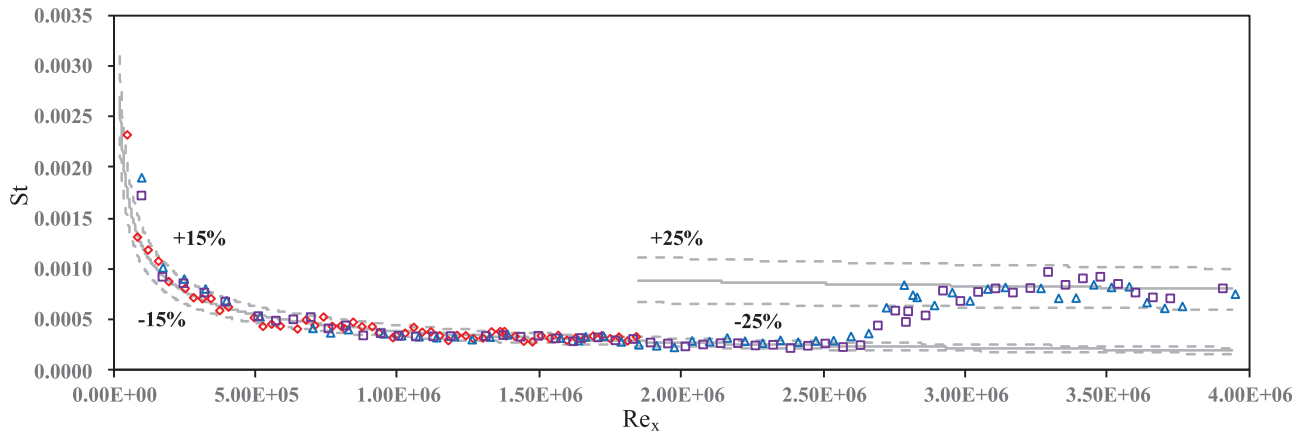
FIG. 9. St distributions for sharp leading-edge flat plate flow. The symbols represent experimental data: $\diamond$ = case I: $Ma = 7.0$, $T_0 = 2120\,K$, $Re_\infty = 6.08 \times 10^5$; $\square$ = case II-1: $Ma = 7.0$, $T_0 = 2220\,K$, $Re_\infty = 1.23 \times 10^6$; $\triangle$ = case II-2: $Ma = 7.0$, $T_0 = 2220\,K$ $Re_\infty = 1.23 \times 10^6$; the gray solid line is the compressible boundary-layer theoretical solution, and the gray dashed line is the error estimation line.

concentrated in the range of 450–800 kHz, and the dominant frequency bands were high-frequency bands. The comparison of the two cases implies that as the unit Reynolds number increased, the bandwidth of the amplitude energy became wider, and the dominant frequency band was also converted from low-frequency bands to high-frequency bands, which corresponds to the enhanced nonlinear effect of disturbance in the boundary layer. Work on the influence of unit Reynolds number on the disturbance evolution in the boundary layer is still in progress. This paper focuses on the analysis of case I in the boundary layer when the most of the disturbances were in the linear evolution stage. The spectral-spatial strip distribution contour reflects the evolution of the power spectrum along the space; as shown in Fig. 11, the structural distribution of the three frequency bands of the mode waves in the boundary layer can be clearly observed. Among them, the bandwidths of the mid/low-frequency bands were narrow, and the energy of the corresponding frequency band was concentrated. In the low-frequency band, there was a continuous energy distribution,

and it was dominant. In the mid-frequency band, there was staged energy distribution. The energy distribution in the high-frequency range was relatively discrete, and it gradually played an important role downstream of the flow field.

The measured pressure fluctuations resulting from the boundary-layer instability waves allowed for the experimental determination of their spatial amplification rates for comparison. The resulting PSD was used to compute the spatial amplification rates $-\alpha_i$. By using the definition of the spatial amplification[66] rate along s, the amplification rate can be calculated as

$$
\begin{aligned}
-\alpha_i\left(f, s_{j+1/2}\right) &= \frac{\ln\left(A(f)_{j+1}/A(f)_j\right)}{s_{j+1} - s_j} \\
&= \frac{1}{2}\frac{\ln\left(PSD(f)_{j+1}/PSD(f)_j\right)}{s_{j+1} - s_j}.
\end{aligned}
\tag{3}
$$

(a)   (b)
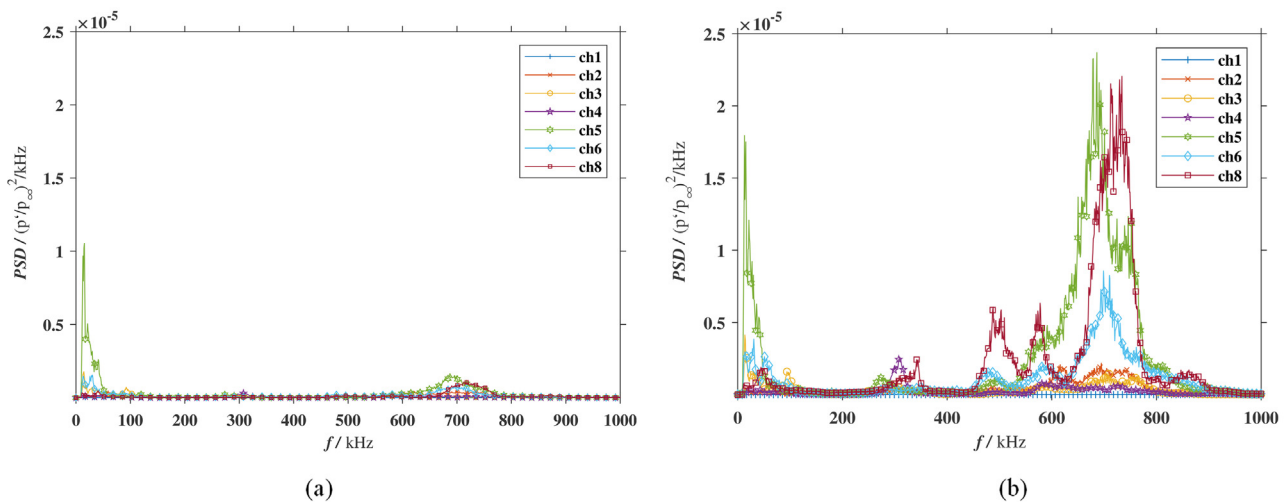
FIG. 10. The PSD distribution diagrams: (a) case I: $Ma = 7.0$, $T_0 = 2120\,K$, $Re_\infty = 6.08 \times 10^5$ and (b) case II: $Ma = 7.0$, $T_0 = 2220\,K$, $Re_\infty = 1.23 \times 10^6$.
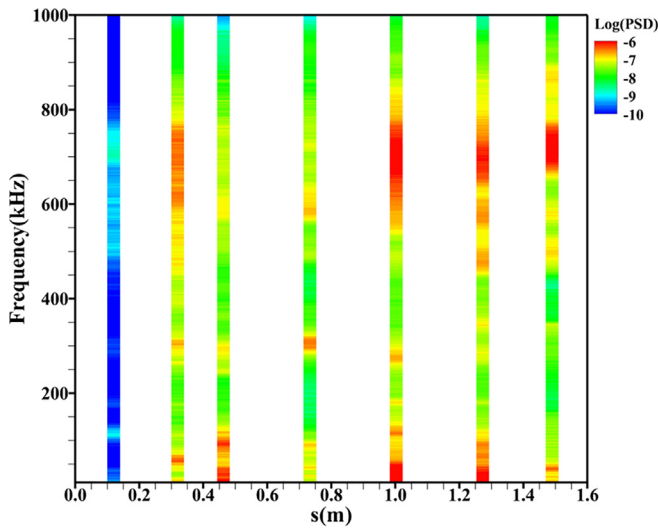
FIG. 11. The PSD spatial distribution contours of case I: Ma = 7.0, T_0 = 2120 K, Re_∞ = 6.08 × 10⁵.

Figure 12 presents the map of the spatial amplification rates ($-\alpha_i$), which merely presents the region of positive amplification to observe the unstable regions. Upstream of the flow field ($s < 0.5$ m), the high-frequency energy was attenuated in area I, and the mid/low-frequency energy was stable. In the middle and downstream of the flow field (0.5 m $< s < 1.2$ m), the low-frequency energy was attenuated in area II. At this point, the mid-frequency energy began to attenuate in area III, lagging behind area II. Downstream of the flow field ($s > 1.2$ m), the mid/low-frequency energy was attenuated, while the high-frequency energy began to increase. In addition, an obvious attenuation band from 600 to 300 kHz was observed. As the flow field developed downstream, the thickness of the boundary layer increased
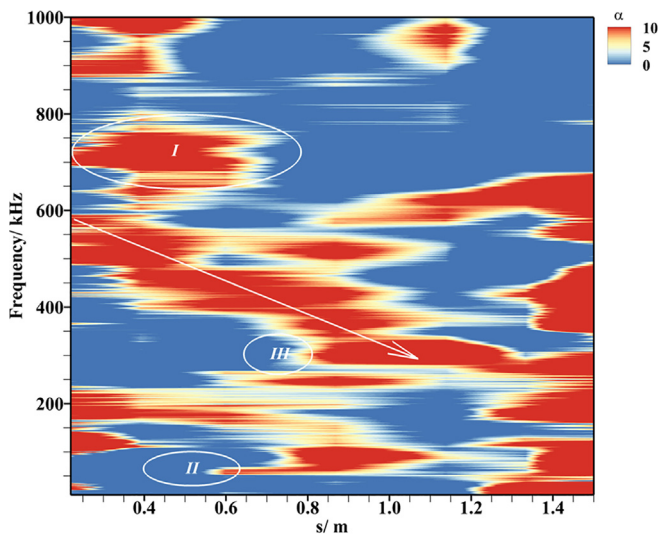
and the position of the sonic line became higher, which caused the peak frequency of the mode wave to shift to the low-frequency direction. During this process, the peak frequency energy exhibited a higher amplitude than the upstream flow field.

C. Temporal evolution of mode waves

Each probe arranged on the model only collected local frequency information, and the accuracy and precision of the frequency information depend on the length of the sampling time. While the steady-state processing method can indeed capture the energy contribution of all frequencies, the temporal evolution information of these frequencies is simultaneously lost. For the processing of unsteady signals, the wavelet transform (WT) method and the short-time Fourier transform (STFT) method were compared, and STFT was ultimately selected to process the signals. As presented in Fig. 13, ch8 could capture the information at all frequencies by analyzing the steady-state signals. The main energy of the signal was concentrated in the high- and low-frequency bands, but the temporal evolution information of the frequency was not known within the effective time. It cannot be judged whether high-frequency waves appeared periodically or persisted. It was also difficult to distinguish whether high-frequency waves were inherently propagated from upstream to downstream, or if they evolved during the propagation process. The frequency (horizontal axis)-time (vertical axis) distribution obtained by STFT is presented in Fig. 14 and reveals that the frequency band of the energy distribution was consistent with Fig. 13. The time resolution of the time-frequency distribution diagram is 1 ms. The amplitude energy of the high-frequency band already existed at the beginning, and the high-frequency energy in the middle time stage underwent fragmentation and integration. In the later stage, the high-frequency energy contributed the most, and the overall evolution exhibited a continuous growth trend with the continuation of time. The amplitude energy of the low-frequency band contributed significantly in the early stage, but with the continuation of time, the low-frequency energy was gradually weakened.
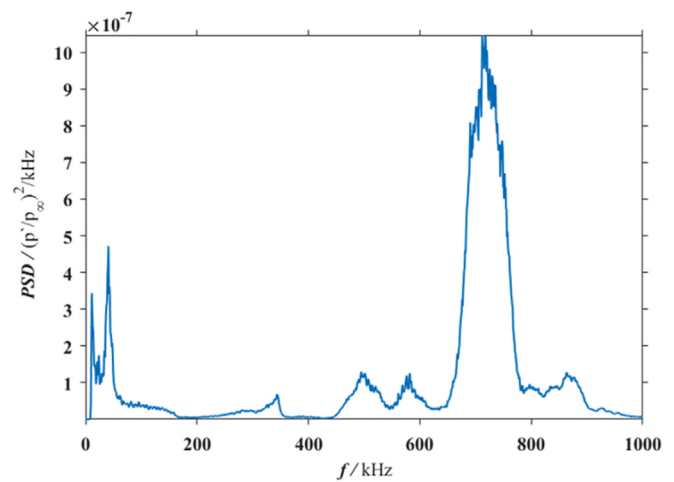

FIG. 12. The spatial amplification rates.

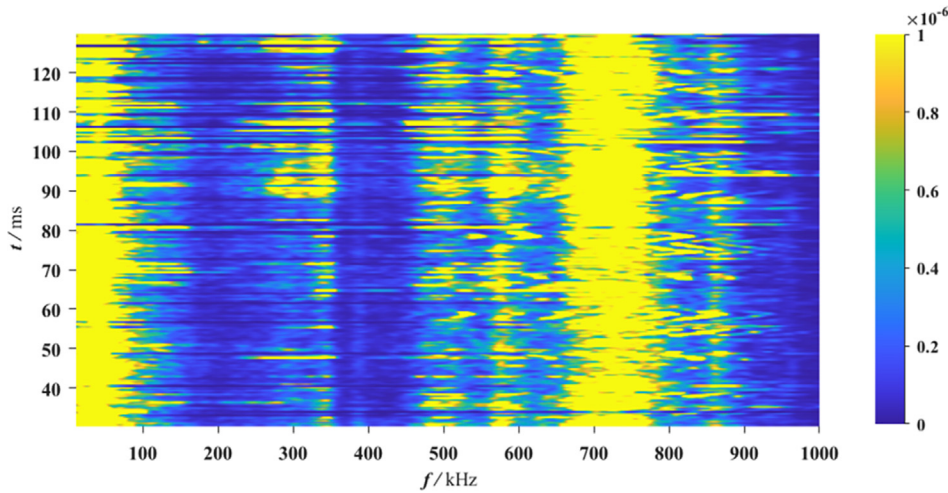**FIG. 13.** The PSD of the ch8 signals.

FIG. 14. The time-frequency distribution diagram of the ch8 signals.

Figure 15 presents the extracted data every 10 ms from the time-frequency diagram to investigate the quantitative evolution of the amplitude energy over time in different frequency bands. The energy corresponding to the peak frequency in the high-frequency band exhibited a fluctuating growth trend, while that in the low-frequency band exhibited a gradually decreasing trend, and the mid-frequency band had no obvious energy contribution. Similarly, the energy corresponding to the peak frequency in the high-frequency band was broken and reintegrated in the middle time stage.

The appropriate bandwidth and integration interval were selected to integrate the high/mid/low-frequency mode waves, and the integration forms are as follows:

$$
\begin{aligned}
Sumpsd &= \sum_{f_i=0}^{F_{cut-off}} PSD(f_i),\\
\%Low\ Frequency &= \sum_{Low\ Frequency\ band} PSD(f_i)/Sumpsd,\\
\%Mid\ Frequency &= \sum_{Mid\ Frequency\ band} PSD(f_i)/Sumpsd,\\
\%High\ Frequency &= \sum_{High\ Frequency\ band} PSD(f_i)/Sumpsd.
\end{aligned}
\tag{4}
$$

The short-time PSD was integrated with a bandwidth of 90 kHz, the integral cutoff frequency $F_{cut-off}$ of the total disturbance energy is 1000 kHz. To eliminate the influence of the sensor response and clearly distinguish the energy contribution of each frequency band, the disturbance energy percentage was used to analyze the evolution of mode waves in different frequency bands. This is because in the laminar stage, the total disturbance energy developed steadily along the space and did not increase significantly. It can be clearly seen through the spatial evolution total disturbance energy in Fig. 16.

Figure 17 presents a series of graphs of the percentage energy contributions of the sensors, and Fig. 17(d) presents the distribution of the percentage energy contributions of the three frequencies corresponding to Fig. 15. The findings imply that the energy contribution percentages of the high- and low-frequency bands presented contrary

trends, and the energy contribution of the mid-frequency band was relatively stable. This phenomenon was universal and captured in all sensors. As shown in Figs. 17(a)–17(c), although the temporal distributions of different frequency bands of different sensors were different, the corresponding high- and low-frequency energy contribution percentages all exhibited contrary trends; this is because, in the entire laminar boundary layer, the total disturbance energy remains stable. However, the disturbance energy was redistributed among the harmonics of various frequency bands. High-frequency harmonics dominate, which means that low-frequency mode waves were broken into high-frequency harmonics, and nonlinear effects began to appear.

D. Spatial evolution of mode waves

The temporal evolution of mode waves reflects the local stability. The dominant frequency is sometimes high-frequency, and sometimes low-frequency. Therefore, it is more worthwhile to analyze the spatial
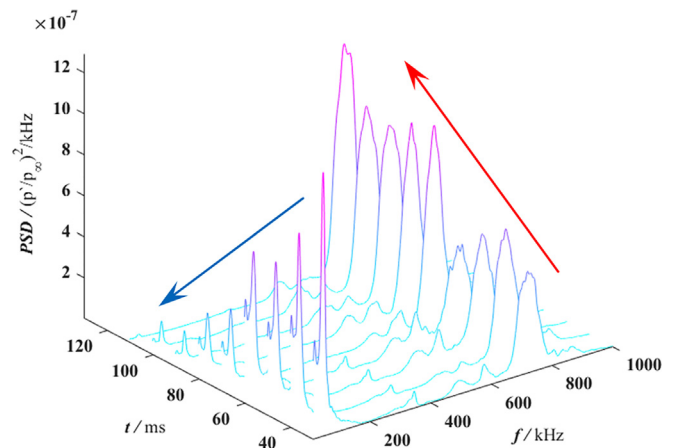

FIG. 15. The PSD diagram of the time station position of the ch8 signals.
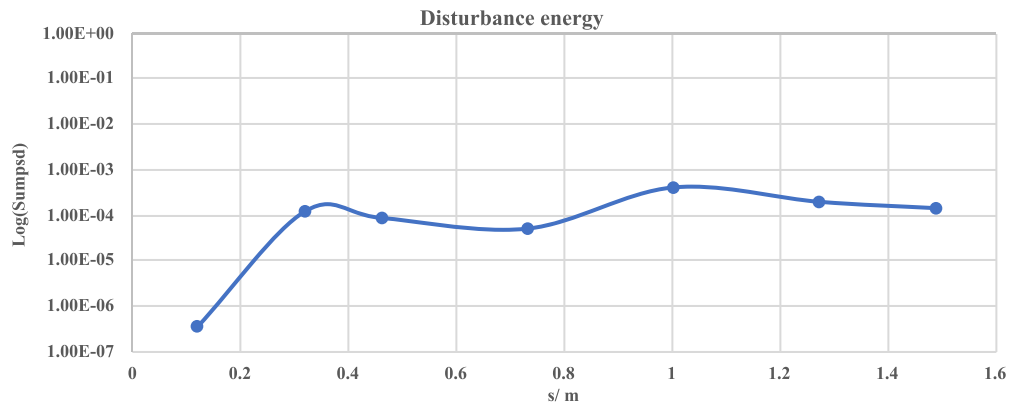
FIG. 16. The spatial distributions of the total disturbance energy.

evolution of mode waves. Via the same calculation method mentioned previously, the spatial evolutions of the PSD, peak frequency, and percentage amplitude energy of the mode waves in the three different frequency bands were analyzed.

For the low-frequency mode waves, according to the PSD distribution, Eq. (4) was used to calculate their PSD percentage distributions, as shown in Fig. 18. To avoid differences caused by the responses of different sensors, the spatial evolution of the mode wave
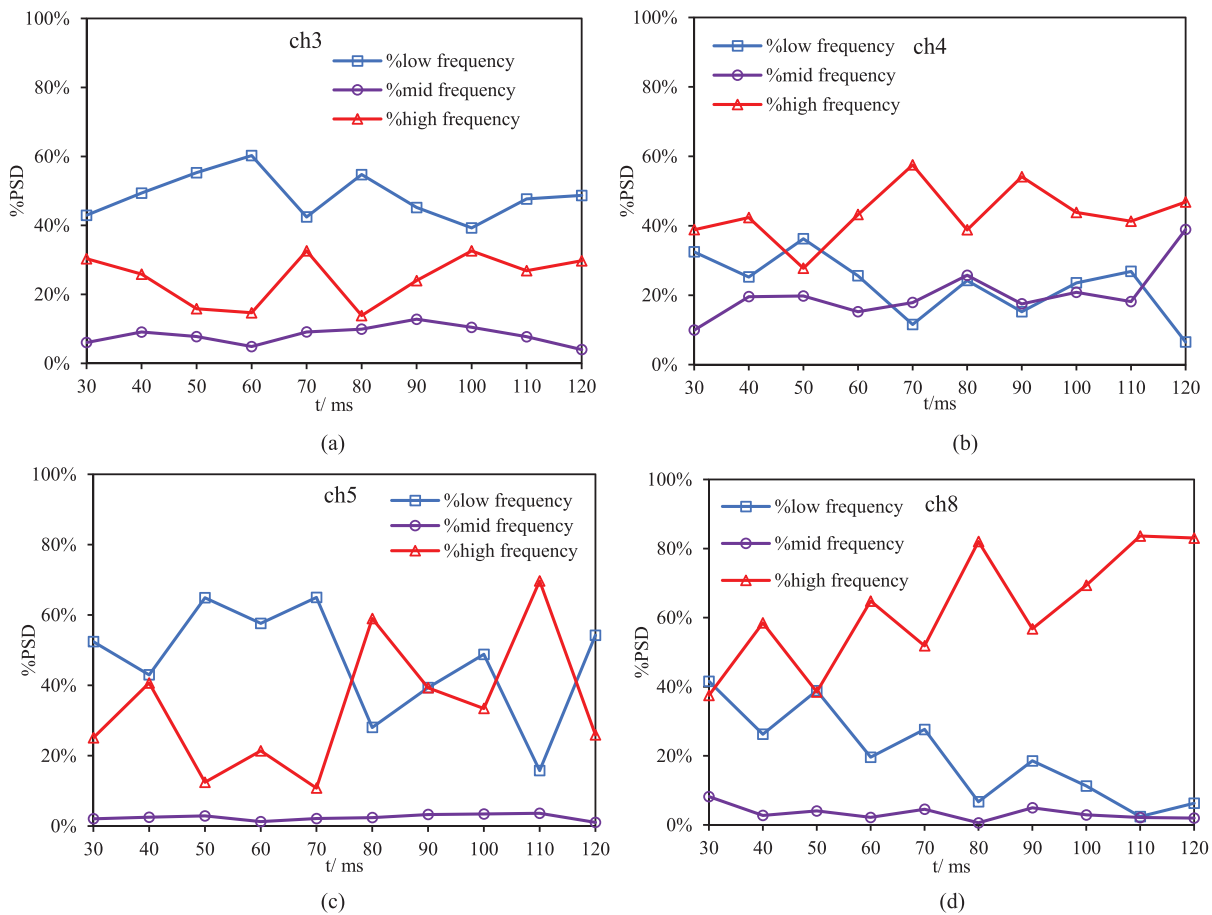

FIG. 17. The percentage energy contribution graphs of sensors (a) ch3, (b) ch4, (c) ch5, and (d) ch8.
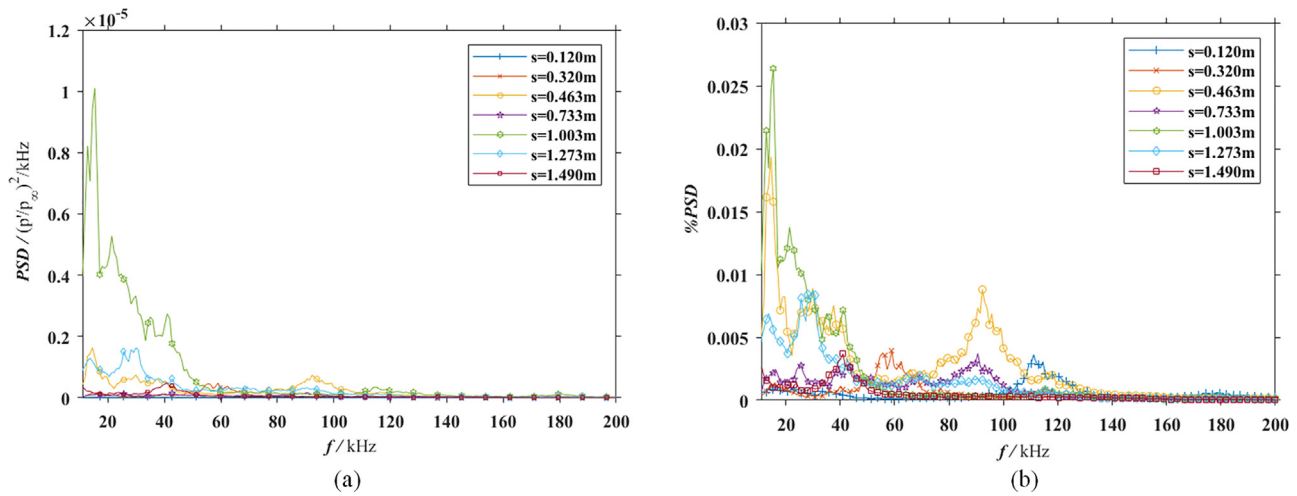
FIG. 18. The spatial distributions of the low-frequency mode waves: (a) PSD distribution and (b) PSD percentage distribution.

was observed with its percentage component. In the low-frequency band, the amplitude was mainly concentrated in the range of 12–50 kHz. When the low-frequency mode waves developed downstream, they did not monotonously increase or attenuate, but broke and integrated in stages.

Therefore, the spatial distributions of the peak frequency and amplitude energy percentage were calculated to further analyze the evolution of low-frequency mode waves. Figure 19 presents the spatial evolution of the dominant frequency; the dominant frequency first experienced accumulation from the high-frequency direction to the low-frequency direction. After that, the low-frequency mode wave dispersed and responded to many harmonics, and the energy distribution was not concentrated. Finally, the peak frequency moved to the high-frequency direction. Figure 24 shows the evolution of the calculated amplitude energy percentage in the 12–102 kHz integration band.
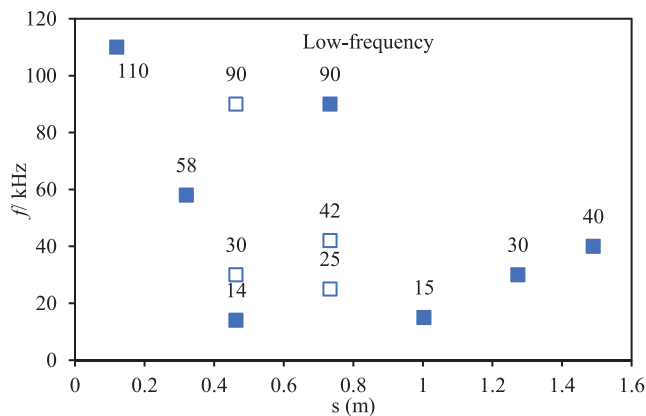
When the dominant frequency accumulated, its energy increased correspondingly, the mode wave dispersion corresponded to a cliff-like drop in its amplitude energy, and the dominant frequency moved to high frequencies, corresponding to the continued decay of the amplitude energy.

For the mid-frequency mode waves, Fig. 20(a) presents the PSD distribution and Fig. 20(b) presents the corresponding PSD percentage distribution. In the mid-frequency band, the amplitude was mainly concentrated in the range of 250–350 kHz, and the energy distribution was concentrated. During the downstream evolution process of the mid-frequency mode waves, a phased increase was revealed, but the growth trend lagged behind the appearance of the low-frequency mode wave. Further, the spatial distributions of the peak frequency and amplitude energy percentage were analyzed. Figure 21 presents the spatial evolution of the dominant frequency, which was found to be stable. Moreover, the peak frequency and harmonic frequency of the mid-frequency band were concentrated around 300 kHz. Figure 24 exhibits the evolution of the calculated amplitude energy percentage in the 255–345 kHz integration band, which was found to be relatively stable. It is worth noting that when the low-frequency mode wave exhibited dispersion, the mid-frequency mode wave responded with greater energy. In the subsequent development process downstream, the energy continued to decay.

For the high-frequency mode waves, Fig. 22(a) exhibits the PSD distribution and Fig. 22(b) exhibits the corresponding PSD percentage distribution. The high-frequency mode waves reflect the nonlinear effect in the evolution of the disturbance. Additionally, the spatial evolution of the high-frequency mode waves was more complicated. In the high-frequency band, the amplitude was mainly concentrated in the range of 650–800 kHz, and the energy distribution was dispersed. During the downstream evolution process of the high-frequency mode waves, they gradually played an important role, indicating that the evolution of disturbances in the boundary layer gradually tended to be nonlinear. Table III lists the dominant frequencies of the

FIG. 19. The spatial evolution of the dominant frequency in the low-frequency band. Symbols represent frequency: ■ = peak frequency in the low-frequency band; □ = harmonic frequency in the low-frequency band.
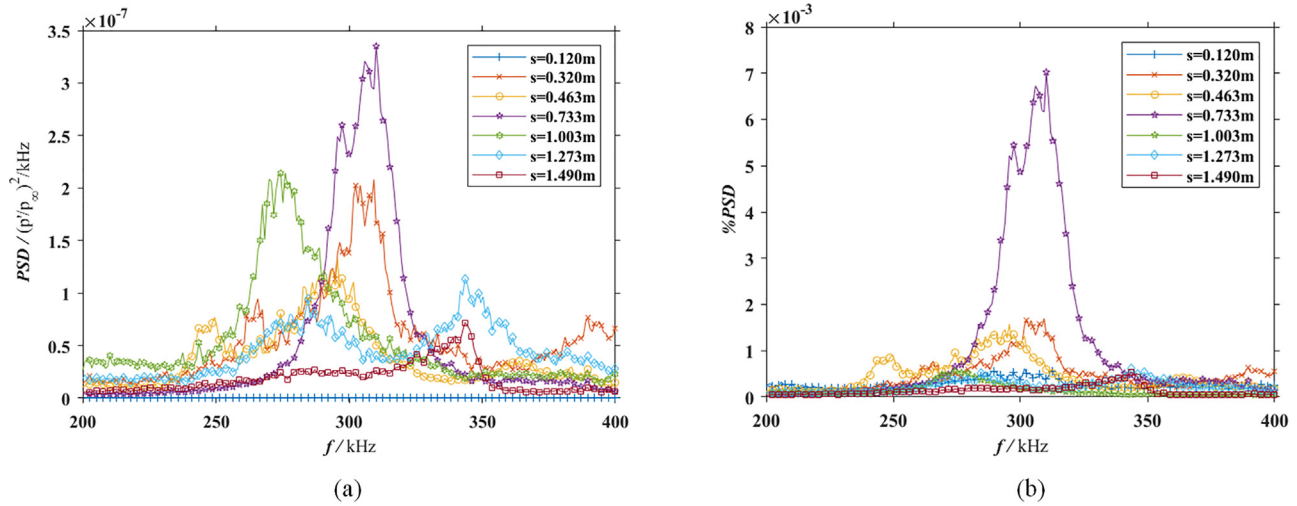
FIG. 20. The spatial distributions of mid-frequency mode waves: (a) PSD distribution and (b) PSD percentage distribution.

high-frequency mode waves and the calculated energy components in different integration bands. Because the energy distribution of high-frequency mode waves is discrete, the integration frequency band selected here is not a fixed frequency band, but a window that varies with the peak frequency. Figure 23 exhibits the spatial evolution of the dominant frequency; the dominant frequency was found to first experience accumulation from the high-frequency direction to the low-frequency direction, and the peak frequency finally moved to the high-frequency direction. The turning point of the dominant frequency evolution was the dispersion position of the low-frequency mode wave. Figure 24 shows the spatial evolution of the amplitude energy percentage; the amplitude energy evolution trend of the high-frequency mode waves was found to be contrary to that of the low-frequency mode waves.

To observe the spatial distributions of the mode waves in the three frequency bands, Fig. 24 presents the percentage components of the integration results of the PSD in different frequency bands. The spatial distribution of the percentage components can better reflect the evolution of the mode waves, as the influence of the sensor response is eliminated. The evolution trends of the low/high-frequency bands were contrary. The spatial distributions of the energy components of the mode waves corresponding to the three frequency bands can be roughly divided into the following three stages: (1) *The low-frequency mode wave energy accumulation stage*. At this stage, the main peak frequencies of the low/high-frequency bands move to the lower frequency direction; the low-frequency energy increases, the high-frequency energy decreases, and the mid-frequency energy stabilizes. (2) *The low-frequency mode wave energy attenuation stage*. At this stage, the low-frequency mode wave has no main peak frequency and responds with more harmonics. The peak frequency of the high-frequency mode wave increases; the low-frequency energy decreases, the high-frequency energy increases, and the mid-frequency energy responds to a phased peak. (3) *The low-frequency mode wave continues to break*. At this stage, the main peak frequencies of the low/high-frequency bands all move to the higher frequency direction; the low-frequency energy continues to decrease, the high-frequency energy increases, and the mid-frequency energy is stable.

IV. CONCLUSIONS

In this research, the flow-field characteristics of the boundary-layer transition of a large-scale flat plate were analyzed, and the fine heat transfer and fluctuating pressure evolution during the boundary-layer transition were determined. The main conclusions of this work are summarized as follows:

(1) The spatial distribution of heat transfer was used to distinguish the transition. In case I (Ma = 7.0, T_0 = 2120 K, Re_∞ = 6.08
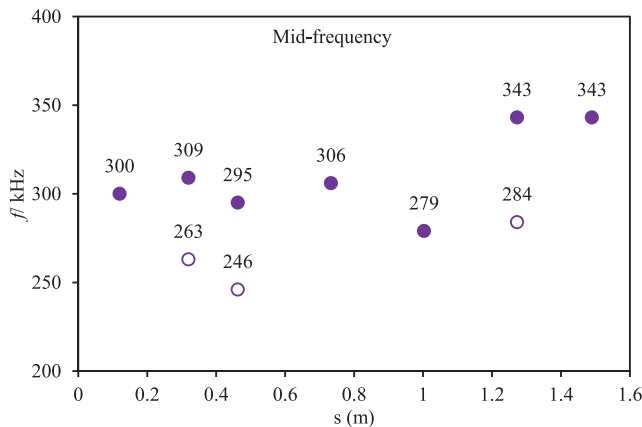

FIG. 21. The spatial evolution of the dominant frequency in the mid-frequency band. Symbols represent frequency: ● = peak frequency in the mid-frequency band; ○ = harmonic frequency in the mid-frequency band.
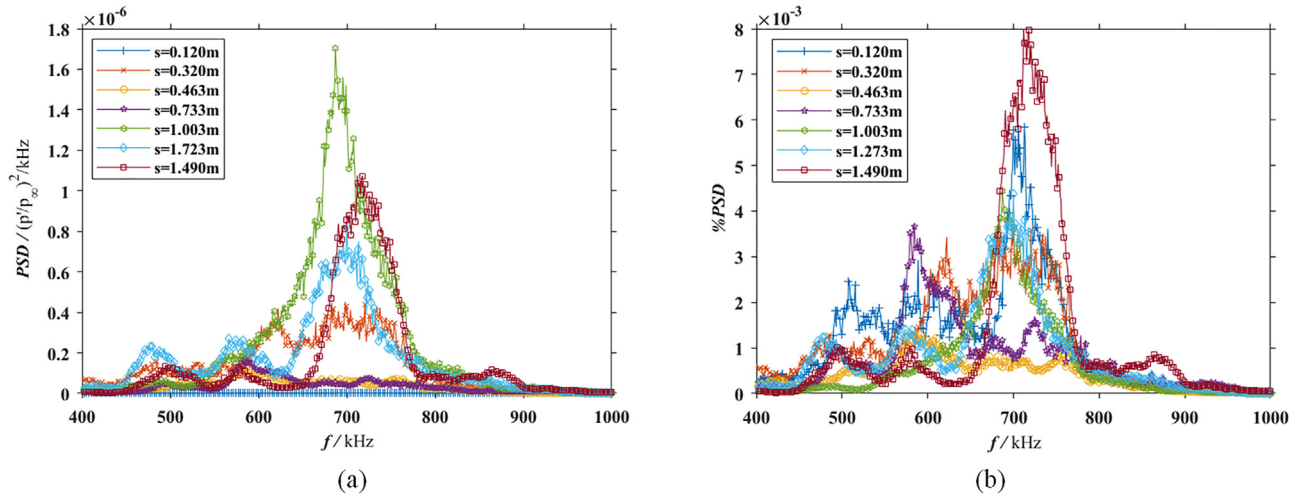
FIG. 22. The spatial distribution of high-frequency mode waves: (a) PSD distribution and (b) PSD percentage distribution.

TABLE III. The evolution parameters of high-frequency mode waves.

Sensor	ch1	ch2	ch3	ch4	ch5	ch6	ch8
Location (m)	0.120	0.320	0.463	0.733	1.003	1.273	1.490
High-frequency (kHz)	700	700/610	595	583/488	695	705/586	715/579/501
Integration band (kHz)	655–745	655–745	550–640	538–628	650–740	660–750	670–760
Amplitude component (%)	74.6%	68.2%	24.4%	45.0%	43.7%	55.2%	75.1%

$\times 10^5$), the entire flat plate was in full laminar flow. In case II (Ma = 7.0, T_0 = 2220 K, Re_∞ = 1.23 × 10⁶), natural transition occurred in the flow, and the transition Reynolds number Re_x = 2.6 × 10⁶. The repeatability of the experiment was good.
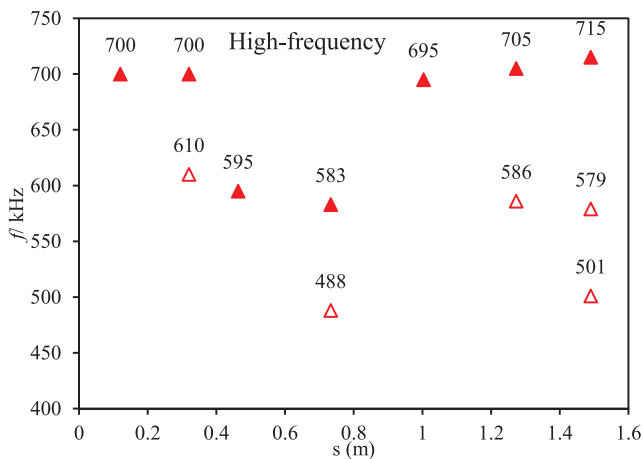

FIG. 23. The spatial evolution of the dominant frequency in the high-frequency band. Symbols represent frequency: ▲ = peak frequency in the high-frequency band; △ = harmonic frequency in the high-frequency band.

Further, the value of Re_∞ was not found to affect the St distribution in the laminar stage.

(2) The experiment captured the three frequency distributions of mode waves in the laminar stage. Among the mode waves distributed in the three frequency bands, the low/high-frequency bands were found to be dominant, but the corresponding mode waves did not increase and decay regularly during the evolution of the boundary layer along the space and time. The mid-frequency band exhibited a staged contribution, and the frequency shift phenomenon also started from the higher frequency band.

(3) The 130 ms effective experiment time of the JF-12 hypersonic duplicated tunnel allowed for the analysis of the temporal evolution of mode waves. The amplitude energy percentages of the high- and low-frequency mode waves exhibited opposite temporal and spatial trends in the laminar flow region of the boundary layer. The attenuation of low-frequency mode wave energy corresponded to the increase in the high-frequency mode wave energy, and vice versa. In the entire laminar boundary layer, the total disturbance energy remains stable, and it was redistributed among the harmonics of various frequency bands. High-frequency harmonic energy has dominated the downstream of the flow field, which means that the evolution of disturbance waves has begun to tend to the stage of non-linear evolution.
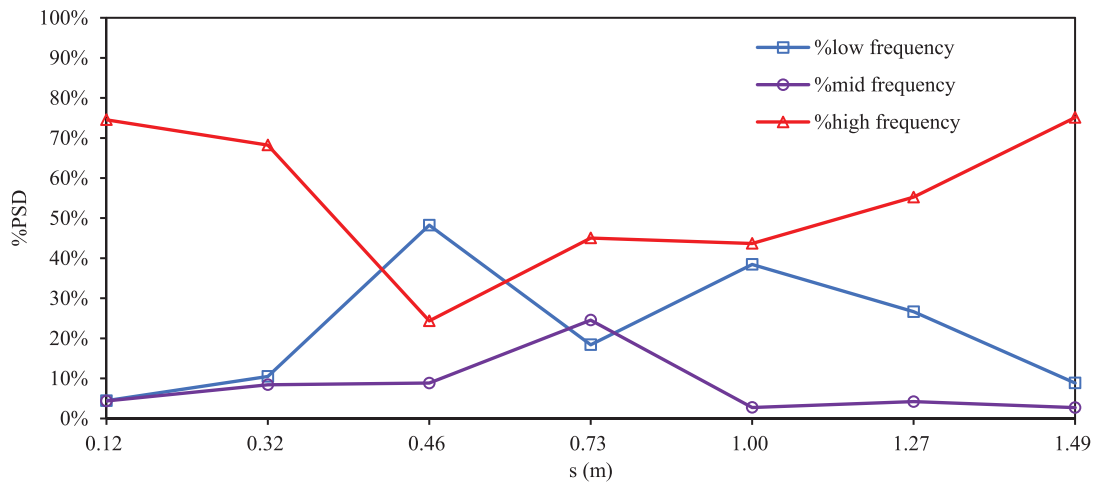
FIG. 24. The spatial distributions of the amplitude energy in the three frequency bands.

ACKNOWLEDGMENTS

AUTHOR DECLARATIONS
Conflict of Interest

The authors report no conflict of interest.

DATA AVAILABILITY

The data that support the findings of this study are available from the corresponding author upon reasonable request.

REFERENCES

[1]E. R. V. Driest, "Investigation of laminar boundary layer in compressible fluid using the Crocco method," National Advisory Committee for Aeronautics, Technical Note No. 2597, 1952.

[2]I. Tani, "Boundary-layer transition," Annu. Rev. Fluid Mech. **1**, 169 (1969).

[3]V. G. Pridanov, A. M. Kharitonov, and V. V. Chernykh, "Combined influence of the mach and Reynolds numbers on transition in the boundary layer," Fluid Dyn. **9**, 126 (1975).

[4]J. J. D. Anderson, *Hypersonic and High-Temperature Gas Dynamics* (AIAA, 2006).

[5]J. E. Gronvall, H. B. Johnson, and G. V. Candler, "Boundary-layer stability analysis of the high enthalpy shock tunnel transition experiments," J. Spacecr. Rockets **51**, 455 (2014).

[6]L. M. Mack, "Stability of axisymmetric boundary layers on sharp cones at hypersonic Mach numbers," AIAA Paper No. 87-1413, 1987.

[7]L. M. Mack, "Transition and laminar instability," NASA Report No. 77-15, 1977.

[8]B. C. Chynoweth, S. P. Schneider, C. Hader, H. Fasel, A. Batista, J. Kuehl, T. J. Juliano, and B. M. Wheaton, "History and progress of boundary-layer transition on a Mach-6 flared cone," J. Spacecr. Rockets **56**, 333 (2019).

[9]J. J. Kuehl, "Thermoacoustic interpretation of second-mode instability," AIAA J. **56**, 3585 (2018).

[10]F. Alexander, "Transition and stability of high-speed boundary layers," Annu. Rev. Fluid Mech. **43**, 79 (2011).

[11]D. Arnal and G. Casalis, "Laminar-turbulent transition prediction in three-dimensional flows," Prog. Aerosp. Sci. **36**, 173 (2000).

[12]A. Klothakis, S. S. Sawant, H. Quintanilha, V. Theofilis, and D. A. Levin, "Slip effects on the stability of supersonic laminar flat plate boundary layer," AIAA Paper No. 2021-1659, 2021.

[13]Y. Jiao, Y. Hwang, and S. I. Chernyshenko, "Orr mechanism in transition of parallel shear flow," Phys. Rev. Fluids **6**, 023902 (2021).

[14]S. Esquieu, E. Benitez, S. P. Schneider, and J. P. Brazier, "Flow and stability analysis of a hypersonic boundary layer over an axisymmetric cone cylinder flare configuration," AIAA Paper No. 2019-2115, 2019.

[15]V. Wartemann, A. Wagner, R. Wagnild, F. Pinna, F. Miró Miró, H. Tanno, and H. Johnson, "High-enthalpy effects on hypersonic boundary-layer transition," J. Spacecr. Rockets **56**, 347 (2019).

[16]J. Sivasubramanian and H. F. Fasel, "Numerical investigation of the development of three-dimensional wavepackets in a sharp cone boundary layer at Mach 6," J. Fluid Mech. **756**, 600 (2014).

[17]X. Li, D. Fu, and Y. Ma, "Direct numerical simulation of hypersonic boundary layer transition over a blunt cone with a small angle of attack," Phys. Fluids **22**, 025105 (2010).

[18]S. Sharma, M. S. Shadloo, and A. Hadjadj, "Laminar-to-turbulent transition in supersonic boundary layer: Effects of initial perturbation and wall heat transfer," Numer. Heat Transfer Appl. **73**, 583 (2018).

[19]P. Hall, "An instability mechanism for channel flows in the presence of wall roughness," J. Fluid Mech. **899**, R2 (2020).

[20]J. M. F. Peter and M. J. Kloker, "Direct numerical simulation of supersonic film cooling by tangential blowing," Document No. 40, 2018.

[21]X. Zhong, "Numerical simulation of hypersonic boundary layer receptivity and stability on blunt circular cones," AIAA Paper No. 2009-940, 2009.

[22]X. Zhong and X. Wang, "Direct numerical simulation on the receptivity, instability, and transition of hypersonic boundary layers," Annu. Rev. Fluid Mech. **44**, 527 (2012).

[23]M. Leinemann, C. Hader, and H. F. Fasel, "Direct numerical simulations of the nonlinear boundary layer transition regime on a flat plate at Mach 6," AIAA Paper No. 2021-1739, 2021.

[24]C. Kumar and A. Prakash, "Secondary subharmonic instability of hypersonic boundary layer in thermochemical equilibrium over a flat plate," Phys. Fluids **33**, 024107 (2021).

[25]Y. Xiong, T. Yu, L. Lin, J. Zhao, and J. Wu, "Nonlinear instability characterization of hypersonic laminar boundary layer," AIAA J. **58**, 5254 (2020).

[26]W. Si, G. Huang, Y. Zhu, S. Chen, and C. Lee, "Hypersonic aerodynamic heating over a flared cone with wavy wall," Phys. Fluids **31**, 051702 (2019).

[27]Y. Zhu, X. Chen, J. Wu, S. Chen, C. Lee, and M. Gad-El-Hak, "Aerodynamic heating in transitional hypersonic boundary layers: Role of second-mode instability," Phys. Fluids **30**, 011701 (2018).

[28]C. Zhang, "Experimental observation of the second-mode waves using PIV technique," J. Visualization **21**, 915 (2018).

[29]E. C. Marineau, G. Grossir, A. Wagner, M. Leinemann, R. Radespiel, H. Tanno, B. C. Chynoweth, S. P. Schneider, R. M. Wagnild, and K. M. Casper, "Analysis of second-mode amplitudes on sharp cones in hypersonic wind tunnels," J. Spacecr. Rockets **56**, 307 (2018).

[30]Y. Zhang, C. Li, and C. Lee, "Influence of glow discharge on evolution of disturbance in a hypersonic boundary layer: The effect of second mode," Phys. Fluids **32**, 071702 (2020).

[31]S. G. Mallinson, N. R. Mudford, and S. L. Gai, "Leading-edge bluntness effects in hypervelocity flat plate flow," Phys. Fluids **32**, 046106 (2020).

[32]M. K. Liu, G. L. Han, and Z. L. Jiang, "Experimental investigation on plate boundary layer transition in JF-12 hypersonic shock tunnel," in 32rd ISSW (2019).

[33]C. Lee and X. Jiang, "Flow structures in transitional and turbulent boundary layers," Phys. Fluids **31**, 111301 (2019).

[34]C. Lee and S. Chen, "Recent progress in the study of transition in the hypersonic boundary layer," Nat. Sci. Rev. **6**, 155 (2019).

[35]J. Liu, J. Xu, C. Wang, P. Yu, and J. Bai, "Pressure gradient effects on the secondary instability of Mack mode disturbances in hypersonic boundary layers," Phys. Fluids **33**, 014109 (2021).

[36]Y. Ma and X. Zhong, "Receptivity of a supersonic boundary layer over a flat plate. Part 1. Wave structures and interactions," J. Fluid Mech. **488**, 31 (2003).

[37]Y. Ma and X. Zhong, "Receptivity of a supersonic boundary layer over a flat plate. Part 2. Receptivity to free-stream sound," J. Fluid Mech. **488**, 79 (2003).

[38]K. Ritos, D. Drikakis, I. W. Kokkinakis, and S. M. Spottswood, "Computational aeroacoustics beneath high speed transitional and turbulent boundary layers," Comput. Fluids **203**, 104520 (2020).

[39]K. J. Franko and S. K. Lele, "Breakdown mechanisms and heat transfer overshoot in hypersonic zero pressure gradient boundary layers," J. Fluid Mech. **730**, 491 (2013).

[40]D. Drikakis, K. Ritos, S. M. Spottswood, and Z. B. Riley, "Flow transition to turbulence and induced acoustics at Mach 6," Phys. Fluids **33**, 076112 (2021).

[41]S. P. Schneider, "Flight data for boundary-layer transition at hypersonic and supersonic speeds," J. Spacecr. Rockets **36**, 8 (2011).

[42]D. M. Bushnell, "Scaling: Wind tunnel to flight," Annu. Rev. Fluid Mech. **38**, 111 (2006).

[43]B. Wan, G. Tu, X. Yuan, J. Chen, and Y. Zhang, "Identification of traveling crossflow waves under real hypersonic flight conditions," Phys. Fluids **33**, 044110 (2021).

[44]J. T. Flood, L. Taubert, and S. A. Craig, "First and Mack-mode instabilities in a flat-plate boundary layer at Mach 4," AIAA Paper No. 2020-0361, 2020.

[45]K. M. Casper, S. J. Beresh, J. F. Henfling, R. W. Spillers, B. O. M. Pruett, and S. P. Schneider, "Hypersonic wind-tunnel measurements of boundary-layer transition on a slender cone," AIAA J. **54**, 1250 (2016).

[46]S. S. Sattarzadeh and J. H. M. Fransson, "Experimental investigation on the steady and unsteady disturbances in a flat plate boundary layer," Phys. Fluids **26**, 124103 (2014).

[47]Q. Tang, Y. Zhu, X. Chen, and C. Lee, "Development of second-mode instability in a Mach 6 flat plate boundary layer with two-dimensional roughness," Phys. Fluids **27**, 064105 (2015).

[48]C. Li, Y. Zhang, and C. Lee, "Influence of glow discharge on evolution of disturbance in a hypersonic boundary layer: The effect of first mode," Phys. Fluids **32**, 071702 (2020).

[49]Z. Jiang and H. Yu, "Aerodynamic Testing at duplicating hypersonic flight conditions with hyper-dragon," in 31st International Symposium on Shock Waves (Springer International Publishing AG, 2019), p. 1.

[50]Z. Jiang, J. Li, Z. Hu, Y. Liu, and H. Yu, "Shock tunnel theory and methods for duplicating hypersonic flight conditions," Chin. J. Theor. Appl. Mech. **50**, 1283 (2018).

[51]Z. Jiang and H. Yu, "Theories and technologies for duplicating hypersonic flight conditions for ground testing," Nat. Sci. Rev. **4**, 290 (2017).

[52]Z. Jiang, J. Li, W. zhao, Y. Liu, and H. Yu, "investigating into techniques for extending the test-duration of detonation-driven shock tunnels," Chin. J. Theor. Appl. Mech. **44**, 824 (2012).

[53]Z. Jiang and H. Yu, "Successful development of the long-test-duration hypervelocity detonation-driven shock tunnel," in 29th ISSW (Springer International Publishing, Switzerland, 2015), p. 51.

[54]H. G. Hornung and G. H. Smith, "The influence of relaxation on shock detachment," J. Fluid Mech. **93**, 225 (1979).

[55]Q. Wang, H. Olivier, H. Einhoff, J. Li, and W. Zhao, "Influence of test model material on the accuracy of transient heat transfer measurements in impulse facilities," Exp. Therm. Fluid Sci. **104**, 59 (2019).

[56]G. M. Corcos, "Resolution of pressure in turbulence," J. Acoust. Soc. Am. **35**, 192 (1963).

[57]W. W. Willmarth, "Corrigendum: Measurements of the fluctuating pressure at the wall beneath a thick turbulent boundary layer," J. Fluid Mech. **21**, 107 (1965).

[58]W. W. Willmarth and C. E. Wooldridge, "Measurements of the fluctuating pressure at the wall beneath a thick turbulent boundary layer," J. Fluid Mech. **14**, 187 (1962).

[59]R. Lueptow, "Transducer resolution and the turbulent wall pressure spectrum," J. Acoust. Soc. Am. **97**, 370 (1995).

[60]C. Alba, K. Casper, S. Beresh, and S. Schneider, "Comparison of experimentally measured and computed second-mode disturbances in hypersonic boundary-layers," AIAA Paper No. 2013-897, 2013.

[61]D. C. Berridge, C. A. C. Ward, R. P. K. Luersen, A. Chou, A. D. Abney, and S. P. Schneider, "Boundary-layer instability measurements in a Mach-6 quiet tunnel," AIAA Paper No. 2012-3147, 2012.

[62]C. A. C. Ward, B. M. Wheaton, A. Chou, P. L. Gilbert, L. E. Steen, and S. P. Schneider, "Boundary-layer transition measurements in a Mach-6 quiet tunnel," AIAA Paper No. 2010-4721, 2010.

[63]J. Li, H. Chen, S. Zhang, X. Zhang, and H. Yu, "On the response of coaxial surface thermocouples for transient aerodynamic heating measurements," Exp. Therm. Fluid Sci. **86**, 141 (2017).

[64]S. Wu, Y. H. Shu, J. P. Li, and H. R. Yu, An Integral Heat Flux Sensor with High Spatial and Temporal Resolutions (Science China Press, 2014).

[65]B. R. Hollis, "User's manual for the one-dimensional hypersonic experimental aero-thermodynamic (1DHEAT) data reduction code," NASA Contractor Report No. 4691, 1995.

[66]E. C. Marineau, G. C. Moraru, D. R. Lewis, J. D. Norris, and J. A. Smith, "Mach 10 boundary layer transition experiments on sharp and blunted cones," AIAA Paper No. 2014-3108, 2014.